Determination of Debye Temperatures and Lamb-Mössbauer Factors for LnFeO3 Orthoferrite Perovskites (Ln = La, Nd, Sm, Eu, Gd)

SCRIMSHIRE, Alex <http://orcid.org/0000-0002-6828-3620>, LOBERA, Alex, BELL, Anthony, JONES, Hywel, STERIANOU, Iasmi <http://orcid.org/0000-0002-0983-7603> and BINGHAM, Paul <http://orcid.org/0000-0001-6017-0798>

Published version

SCRIMSHIRE, Alex, LOBERA, Alex, BELL, Anthony, JONES, Hywel, STERIANOU, Iasmi and BINGHAM, Paul (2018). Determination of Debye Temperatures and Lamb-Mössbauer Factors for LnFeO3 Orthoferrite Perovskites (Ln = La, Nd, Sm, Eu, Gd). Journal of Physics: Condensed Matter, 30 (10).

Determination of Debye Temperatures and Lamb-Mössbauer Factors for $LnFeO_3$ Orthoferrite Perovskites (Ln = La, Nd, Sm, Eu, Gd)

A. Scrimshire[1,*], A. Lobera[1], A. M. T. Bell[1], A. H. Jones[1], I. Sterianou[1], S. D. Forder[1] and P. A. Bingham[1]

[1] Materials and Engineering Research Institute, Faculty of Arts, Computing, Engineering and Sciences, Sheffield Hallam University, Howard Street, Sheffield S1 1WB, UK

* Corresponding author: Email alexscrimshire@gmail.com

Abstract

Lanthanide orthoferrites have wide-ranging industrial uses including solar, catalytic and electronic applications. Here a series of lanthanide orthoferrite perovskites, $LnFeO_3$ (Ln = La; Nd; Sm; Eu; Gd), prepared through a standard stoichiometric wet ball milling route using oxide precursors, has been studied. Characterisation through X-ray diffraction and X-ray fluorescence confirmed the synthesis of phase-pure or near-pure $LnFeO_3$ compounds. ^{57}Fe Mössbauer spectroscopy was performed over a temperature range of 10 K to 293 K to observe hyperfine structure and to enable calculation of the recoil-free fraction and Debye temperature (θ_D) of each orthoferrite. Debye temperatures (Ln = La 474 K; Nd 459 K; Sm 457 K; Eu 452 K; Gd 473 K) and recoil-free fractions (Ln = La 0.827; Nd 0.817; Sm 0.816; Eu 0.812; Gd 0.826) were approximated through minimising the difference in the temperature dependent experimental Centre Shift (CS) and theoretical Isomer Shift (IS), by allowing the Debye temperature and Isomer Shift values to vary. This method of minimising the difference between theoretical and actual values yields Debye temperatures consistent with results from other studies determined through thermal analysis methods. This displays the ability of variable-temperature Mössbauer spectroscopy to approximate Debye temperatures and recoil-free fractions, whilst observing temperature induced transitions over the temperature range observed. X-ray diffraction and Rietveld refinement show an inverse relationship between FeO_6 octahedral volume and approximated Debye temperatures. Raman spectroscopy show an increase in the band positions attributed to soft modes of A_g symmetry, $A_g(3)$ and $A_g(5)$ from La to $GdFeO_3$ corresponding to octahedral rotations and tilts in the [010] and [101] planes respectively.

Key words: Mössbauer Spectroscopy; Debye Temperature; Rare-Earth Orthoferrite; $ReFeO_3$; $LnFeO_3$

1. Introduction

$LnMeO_3$, lanthanide metal oxide perovskites, have attracted considerable attention for a wide variety of potential applications. To highlight a few examples, (La, Sm, Eu, Gd)FeO_3 exhibit photocatalytic properties [1,2]; $LaFeO_3$ can be a

heterogeneous catalyst [3–5]; (La, Sm)FeO_3 thick films have chemical sensing properties [6,7]; and La(Mn,Cr)O_3 has been used for cathodes and interconnects in solid-oxide fuel cells [8]. Fundamental studies of these materials utilising synchrotron techniques have been recently conducted, for example neutron diffraction of $TbFeO_3$ to understand it's multiferroic nature [9]; and of $NdFeO_3$ to understand temperature induced spin reorientation and structural changes [10]. In recent years there have been a number of lengthy review articles of perovskite oxides in the interests of ferroelectricity [11], piezoelectricity [12], environmental catalysts [13] and for solar cell applications [14,15]. Advantages of perovskite ceramics over conventional materials are often cited as their lower price, facile synthesis routes and ability to be compositionally tailored to suit the application.

$LnFeO_3$ perovskites have distorted orthorhombic structures [16], wherein the Fe^{3+} is co-ordinated with 6 oxygen as FeO_6 octahedra [17] and the larger Ln^{3+} cation is co-ordinated with 12 oxygen atoms, as illustrated schematically for $GdFeO_3$ in Figure 1. These materials have been studied extensively, using Raman spectroscopy [18,19], X-ray diffraction [20,21] and Mössbauer spectroscopy [3,5,17] amongst other techniques, to characterise their vibrational, structural, electronic and magnetic properties. Advances in synthesis techniques and the more recent ability to prepare supported perovskites [22,23], coupled with the wide range of applications for these materials, are motivations behind this present work.

In this work, variable temperature ^{57}Fe Mössbauer spectroscopy has been used to approximate the Debye temperature and recoil-free fractions of five rare-earth orthoferrites. More than a comparative investigation of lanthanides, the findings of this study will provide useful information for further studies in which these materials may act as a baseline for changes to nominal composition or structure, synthesis routes, support matrices and post-processing treatments.

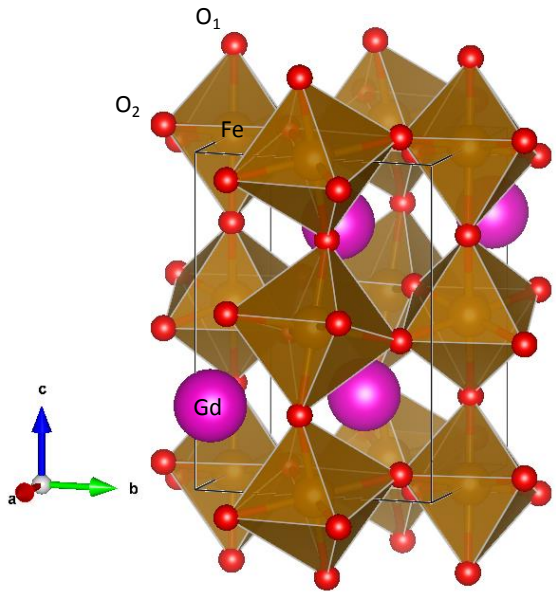

Figure 1. Polyhedral schematic of $GdFeO_3$ orthorhombic perovskite unit cell rendered in VESTA © [24,25]. Lattice parameters are shown in Table 1.

2. Experimental Procedures

2.1 Perovskite synthesis

Conventional solid-state ceramic synthesis of $LnFeO_3$ (Ln = La, Nd, Sm, Eu, Gd) materials was carried out, using Fe_2O_3 (98%, Alfa Aesar) and either La_2O_3 (>99.9%, Arcos Organics), Nd_2O_3 (>99.9%, Arcos Organics), Sm_2O_3 (>99.9%, Alfa Aesar) Eu_2O_3 (>99.9% Alfa Aesar), or Gd_2O_3 (99.99%, Strem Chemicals). Other synthesis routes have been reported for $LnFeO_3$ perovskite oxides, including flame spray pyrolysis, microwave crystallisation and auto combustion [5,17,26], and the physical properties of the perovskites are known to be dependent on the synthesis method [13,27]. Solid-state sintering was utilised for this work to produce dense monoliths and to avoid particle-size induced variables. To prepare 100 g of $LnFeO_3$, dried (>48 h, 120 °C), Ln_2O_3 and Fe_2O_3 precursors were weighed in the required 1:1 molar ratios. These powders were placed in a 250 ml polyethylene bottle with ≈ 500 g of yttrium-stabilised zirconia (YSZ) milling media and ≈ 100 ml of propan-1-ol, and then were milled using a roller ball mill for 24 hours. The resultant slurries were air dried and subsequently calcined in an electric furnace in air at 800 °C for 24 hours before being sieved through a 75 µm mesh. The process, from milling, was repeated for a second time, after which 10 mm diameter green compacts were made by uniaxial pressing under applied pressure of ≈ 3 tonnes for 90 seconds. Green compact pellets were then fired in an electric furnace in air using a controlled heating rate of 5 °C /min, followed by holding for 4 hours at a temperature of 1200 °C, following which the pellets were cooled inside the furnace. After sintering, the pellets were powdered using a manual pestle and mortar, and sieved to a particle size < 75 µm.

2.2 X-ray Fluorescence

Elemental analysis was performed using a PANalytical MagiX Pro X-ray Fluorescence (XRF) spectrometer equipped with a Rh anode. Powdered samples were mixed with cellulose binder and pressed into pellets using a 20 tonne force in a Retsch PP40 hydraulic press. For this XRF spectrometer, Na is usually the lightest element detectable, and any unexpected Rh lines observable are attributed to the anode x-ray source. Accuracies of the resultant data in this study are estimated to be ± 0.2 % of the values provided by the analysis.

2.3 X-ray diffraction

Phase identification was performed using room temperature powder X-ray diffraction on powdered pellets using an Empyrean PANalytical diffractometer in Bragg-Brentano geometry. Samples were mounted on a reflection / transmission spinner stage rotating at 15 rpm, irradiated with Cu K_α radiation (λ = 1.5406 Å) over a $^\circ 2\theta$ range of 20 to 80 degrees, with step size 0.013 $^\circ 2\theta$ and step time 68.59 seconds, 10 mm incident mask, 1° anti-scatter and divergence slits, and a nickel beta filter. X-rays were detected using a PIXCEL-3D area detector. Phases were identified by fingerprinting against the ICDD database using the PANalytical software, X'Pert HighScore Plus. Crystal structures of the $LnFeO_3$ perovskites were refined by the Rietveld method [28] using FULLPROF software [29].

2.4 Raman Spectroscopy

Raman spectroscopy measurements were carried out using a Thermo Scientific DXR2 spectrometer with a depolarised 10 mW 532 nm laser, on powdered samples of the synthesised materials, between 200 and 2000 cm^{-1}. Calibrations with the proprietary Thermo alignment tool were carried out before, during and after each sample measurement.

2.5 ^{57}Fe Mössbauer Spectroscopy

For transmission ^{57}Fe Mössbauer spectroscopy measurements, acrylic absorber discs with a sample area of 1.767 cm^2 were loaded to present 2.16 x 10^{-3} g/cm^2 of Fe to achieve a Mössbauer thickness of 1 [30]. Sample weights of 0.013 g were homogeneously mixed with graphite to achieve this level of loading. The 14.4 keV γ-rays were supplied by the cascade decay of 25 mCi ^{57}Co in Rh matrix source, oscillated at constant acceleration by a SeeCo W304 drive unit, and detected using a SeeCo 45431 Kr proportional counter operating with 1.745 kV bias voltage applied to the cathode. All measurements were carried out over a velocity range of +/- 12 mm s^{-1} due to the presence of high-field magnetic splitting, and were calibrated relative to α-Fe foil. Spectral data were fitted using the Recoil software package [31], using Lorentzian line shapes. Sub-ambient temperatures were maintained using a Janis 10 K CCR cytostatic spectrometer (Model CCS-800/204N) and Lakeshore 335 temperature controller.

3. Results

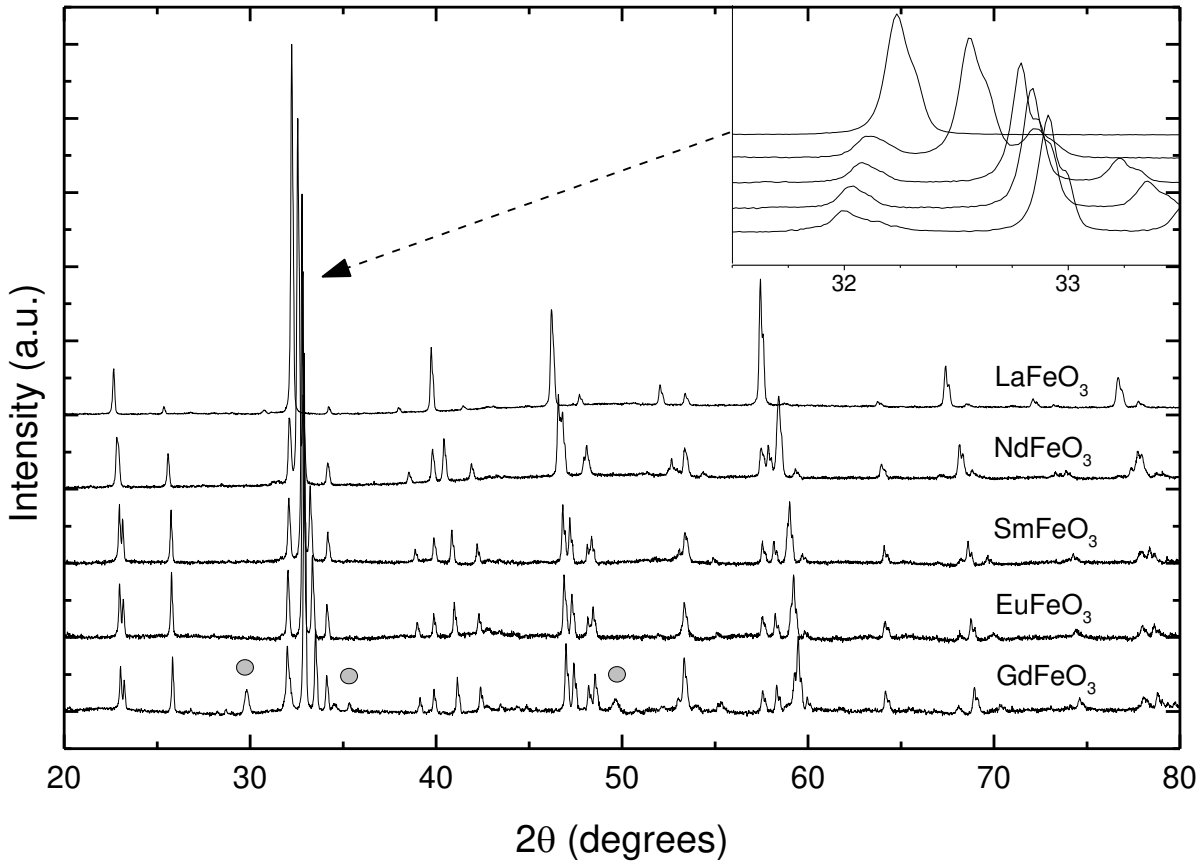

Figure 2. X-ray diffractogram of $LnFeO_3$ series (La to Gd, top to bottom). Circles indicate second phase.

Table 1. Lattice parameters of $LnFeO_3$ perovskites refined by Rietveld refinement from referenced starting structures.

$LnFeO_3$	$LaFeO_3$	$NdFeO_3$	$SmFeO_3$	$EuFeO_3$	$GdFeO_3$
a (Å)	5.55531(16)	5.45509(8)	5.40201(8)	5.37715(8)	5.35188(9)
b (Å)	5.5602(2)	5.57756(9)	5.59063(8)	5.59319(9)	5.59788(10)
c (Å)	7.85114(19)	7.76423(12)	7.71054(12)	7.68806(12)	7.67091(14)
Vol. (Å^3)	242.511(13)	236.235(6)	232.863(6)	231.222(6)	229.814(7)
R_p	27.9	25.8	31.7	33.0	43.3
R_{wp}	17.5	16.8	18.8	17.6	23.2
R_{exp}	6.77	7.55	10.36	11.18	11.37
χ^2	8.281	5,724	3.856	2.853	4.205
Reference	[32]	[10]	[33]	[34]	[25]
Bond Lengths (Å)					
Fe-O1	1.997(12)	1.985(3)	2.020(5)	2.000(3)	1.979(4)
Fe-O2	1.99(5)	1.968(15)	2.002(16)	1.964(11)	1.969(16)
Fe-O2	1.99(5)	2.016(13)	2.009(16)	2.058(11)	2.064(16)
FeO_6 Volume	10.53 Å^3	10.50 Å^3	10.82 Å^3	10.77 Å^3	10.72 Å^3
Bond Angles (˚)					
Fe-O1-Fe	158.7	155.94	145.28	147.96	151.37
Fe-O2-Fe	162.3	156.5	151.4	149.3	147.5
O – Fe – O	180	180	179.9	180	180

Elemental analysis by XRF (PANalytical MagiX Pro; Rh anode) showed trace amounts (< 1 weight%) of ZrO_2 were present in $LaFeO_3$ and $EuFeO_3$, and 3.3 weight % ZrO_2 in $GdFeO_3$, most from the milling process wherein yttria- stabilised zirconia milling media were used. In the $GdFeO_3$ sample this was clearly identified by XRD as being tetragonal $ZrO_{1.97}$, stabilised at room temperature by yttrium [35].

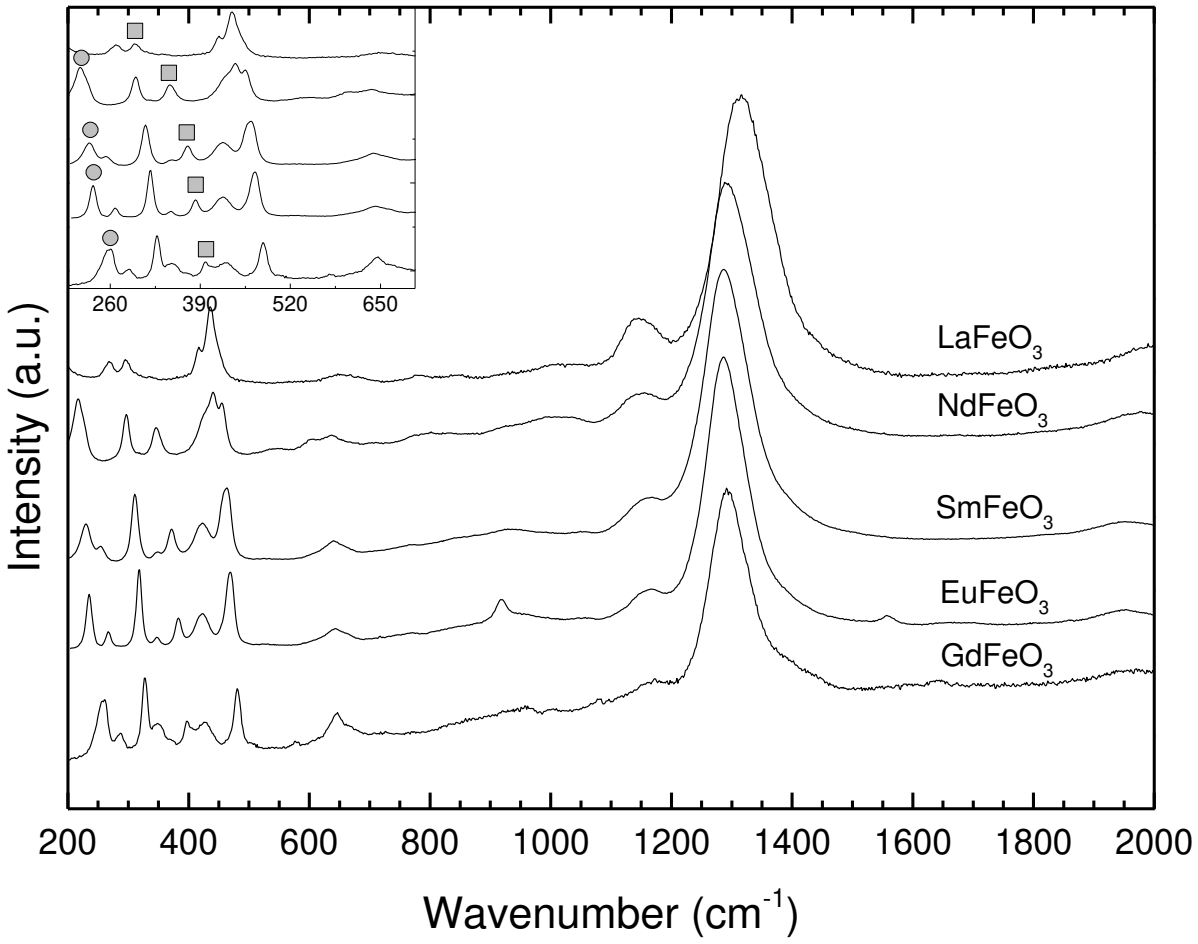

Figure 3. Raman spectra of $LnFeO_3$ series (La to Gd, top to bottom) from 200 to 2000 cm^{-1}, with inset of 200 to 700 cm^{-1}; circles indicate $A_g(3)$ mode and squares indicate $A_g(5)$

Table 2. Raman vibrational peak centres (in cm^{-1}) for $LnFeO_3$ perovskites (Ln = La, Nd, Sm, Eu, Gd) measured using a 532 nm laser.

$LaFeO_3$			$NdFeO_3$		$SmFeO_3$		$EuFeO_3$		$GdFeO_3$	
Present Study	[36]	[17]	Present Study	[37]	Present Study	[38]	Present Study	[39]	Present Study	[17]
105	-	101	106	103	229	225	-	140	111	103
140	-	151	140	142	254	260	235	218	158	152
160	154	-	151	153	311	310	267	291	260	246
181	176	173	216	-	349	-	318	-	287	275
268	-	264	297	297	372	375	347	362	328	316
295	284	288	346	349	423	420	383	-	350	-
436	432	431	441	441	464	460	423	445	396	386
651	653	650	455	458	637	630	470	-	430	412
1145	1154	1143	602	-	1166	-	643	-	480	469
1315	1315	1310	637	-	1287	-	917	-	581	-
			1155	-			1166	-	647	623
			1288	-			1287	-	962	-
			1975	-			1556	-	1084	-
									1173	-
									1291	1280

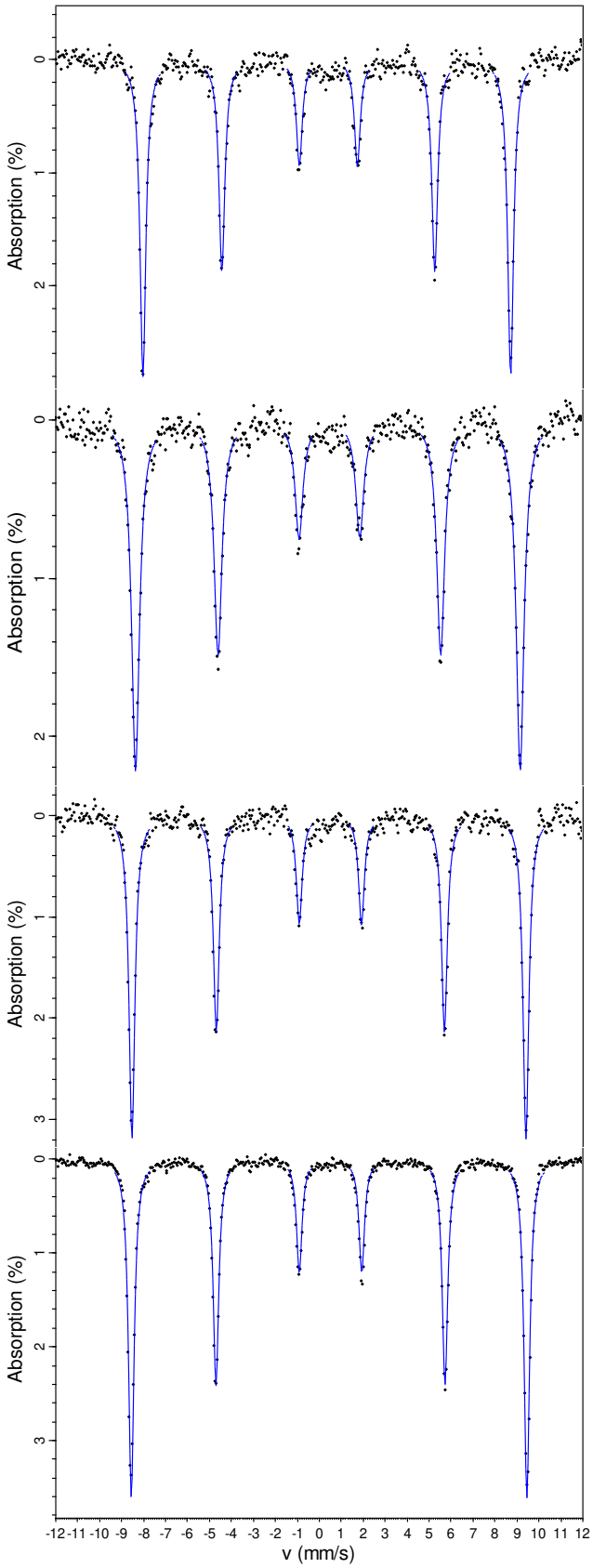

Figure 4. Fitted Mössbauer spectra of $LaFeO_3$ perovskite measured at 293, 200, 100 and 10 K (top to bottom).

Table 3. Hyperfine parameter of single Lorentzian sextets fit for $LnFeO_3$ perovskites. CS given relative to thin α-Fe foil.

Ferrite	Temperature (K)	CS (mm s^{-1})	H (T)	Γ/2 (mm s^{-1})	Reduced X^2
Uncertainty	**[± 1 K]**	**[± 0.02 mm s^{-1}]**	**[± 0.5 T]**	**[± 0.02 mm s^{-1}]**	
$LaFeO_3$	293	0.37	51.9	0.16	1.35
	250	0.39	53.1	0.16	1.38
	200	0.42	54.3	0.21	0.78
	150	0.45	55.1	0.16	1.42
	100	0.46	55.6	0.16	1.35
	80	0.47	55.7	0.15	1.57
	50	0.47	55.8	0.14	1.41
	10	0.48	55.8	0.15	1.43
$NdFeO_3$	293	0.37	51.0	0.15	0.74
	250	0.39	52.5	0.16	0.69
	200	0.42	53.8	0.17	0.87
	150	0.45	54.8	0.16	0.86
	100	0.47	55.3	0.15	0.79
	10	0.48	55.6	0.16	0.82
$SmFeO_3$	293	0.37	50.2	0.16	0.78
	250	0.39	51.7	0.17	0.69
	200	0.43	53.4	0.17	0.47
	150	0.45	54.5	0.15	0.63
	100	0.47	55.1	0.15	0.51
	50	0.48	55.4	0.14	0.65
	10	0.48	55.0	0.16	0.63
$EuFeO_3$	293	0.38	50.2	0.18	1.41
	250	0.40	51.8	0.17	0.97
	200	0.43	53.2	0.18	0.95
	150	0.46	54.3	0.17	0.89
	100	0.48	54.9	0.17	1.16
	50	0.49	55.1	0.16	1.66
	10	0.49	55.2	0.16	0.87
$GdFeO_3$	293	0.36	49.8	0.17	0.80
	250	0.39	51.3	0.18	0.68
	200	0.41	52.8	0.17	0.61
	150	0.44	53.9	0.17	0.64
	100	0.46	54.5	0.15	0.92
	50	0.47	54.8	0.15	0.63
	10	0.47	54.9	0.17	0.69

4. Analysis of Results

4.1 X-ray Diffraction and Rietveld Refinement

XRD analysis confirmed the presence of single-phase $LnFeO_3$ for all rare-earth orthoferrites, except for $GdFeO_3$, as shown in Figure 2. Low levels of mechanical contamination from the milling media were identified by XRD and XRF, however, as this is a mechanical mixture of two materials it would have no appreciable effect on the measured Mössbauer spectrum for this sample since the second phase is iron-free. As the ionic radius of the rare earth cation decreases from 1.36 Å for 12 co-ordinated La^{3+} to 1.22 Å for 12 co-ordinated Gd^{3+} [40], a decrease in unit cell volume is observed by XRD as summarised in Table 1, resulting in a peak shift to higher angles. For all but the $GdFeO_3$ sample, single-phase Rietveld refinements were carried out using isostructural *Pbnm* crystal structures. For $GdFeO_3$ a 2-phase refinement was carried out with $GdFeO_3$ as the main phase [25] and $ZrO_{1.97}$ from the milling media included as a minor phase (7.6(3))% by refinement [41]). Table 1 shows the refined lattice parameters for the $LnFeO_3$ phases, together with the R-factors from the FULLPROF refinements. Figure 5 shows the Rietveld plot of the $GdFeO_3$ sample material, indicating the presence of this second phase and the assignment of diffraction peaks. The phase identification of tetragonal $ZrO_{1.97}$, which is not a stable polymorph of zirconia at room temperature [41], suggests that this structure is being stabilised by a secondary component, most likely Y_2O_3, due to the use of yttrium stabilised zirconia milling media.

From the structures of the $LnFeO_3$ series determined by Reitveld refinement, the largest cell volume is present for $LaFeO_3$, with a consistent decrease in cell volume as the ionic radius of the rare earth decreases from Ln = La to Gd. As the cell volume reduces linearly by ≈ 5.2% from $LaFeO_3$ to $GdFeO_3$, FeO_6 octahedra volume does not vary linearly. We observe that the bonds in the direction of c, or in the [010] plane, connecting FeO_6 octahedra do tend away from 180˚ from La to Sm, however Eu and $GdFeO_3$ exhibit and bonds closer to 180˚, while the O – Fe – O bonds remain essentially 180˚ inside of the octahedra. An inverse relation can be observed between the FeO_6 volume and the bond angles of Fe – O_1 – Fe, while the Fe – O_2 – Fe bond angles reduce almost linearly from 180˚ as the rare earth cation radius decreases. Figure 6 shows the polyhedral schematic of La, Sm and $GdFeO_3$ along the *c* axis, where the octahedra tilting can clearly be observed.

Limitations of site occupancies of perovskite sites, as a function of cation and anion, are indicated by the Goldschmidt tolerance factor [42], shown in equation (1), which predicts crystal structures based on ionic radii. Using Shannon ionic radii [40] tolerance factors of 0.961, 0.929, 0.918, 0.914 and 0.911 for Ln = La, Nd, Sm, Eu and Gd, respectively are calculated. The closer the tolerance factor to 1, the more likely that the crystal structure will exhibit cubic symmetry; structures with tolerance factors > 1 tend towards hexagonal structures and < 1 towards orthorhombic structures [42].

$$t = \frac{r_A + r_X}{\sqrt{2}(r_B + r_X)}$$ Equation (1)

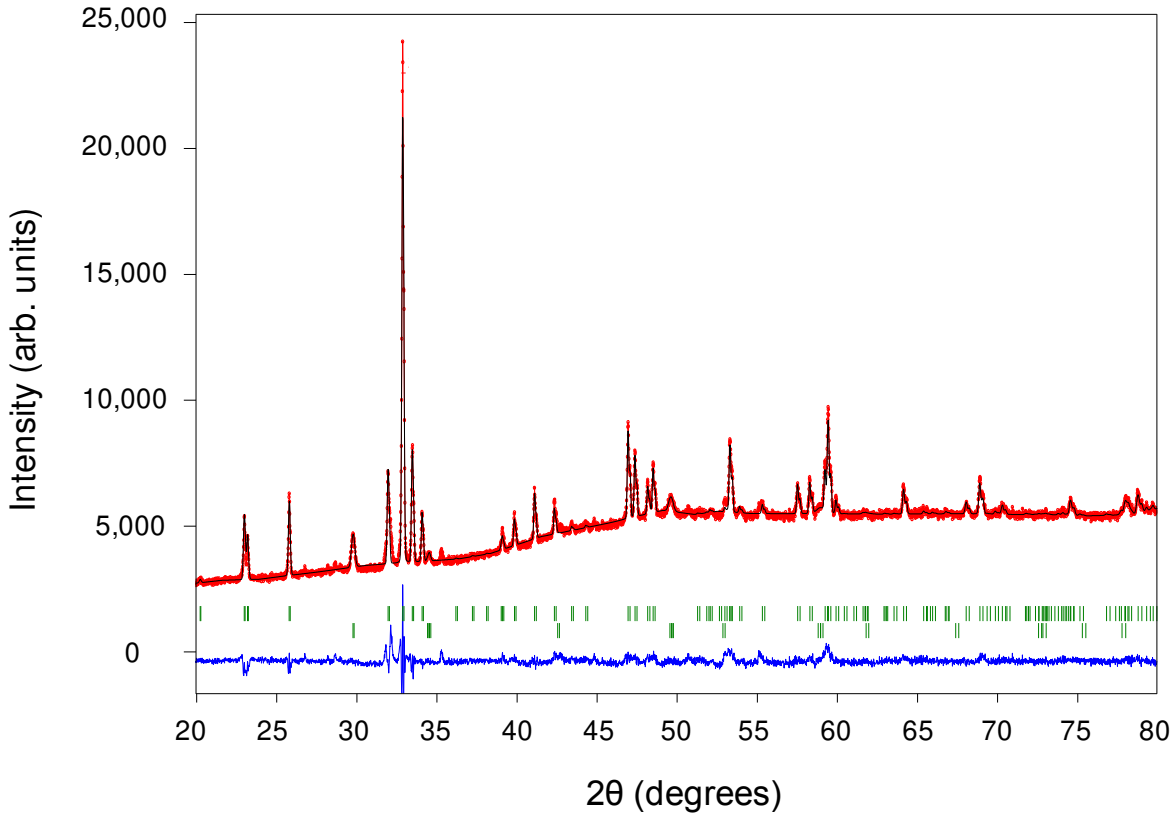

Figure 5. X-ray diffractogram of $GdFeO_3$ with Rietveld refinement using $GdFeO_3$ and $ZrO_{1.97}$ starting structures. Red line indicates observed data, black line indicates calculated data, blue line shows difference between observed and calculated data. Green lines indicate the positions for $GdFeO_3$ (upper) and $ZrO_{1.97}$ (lower).

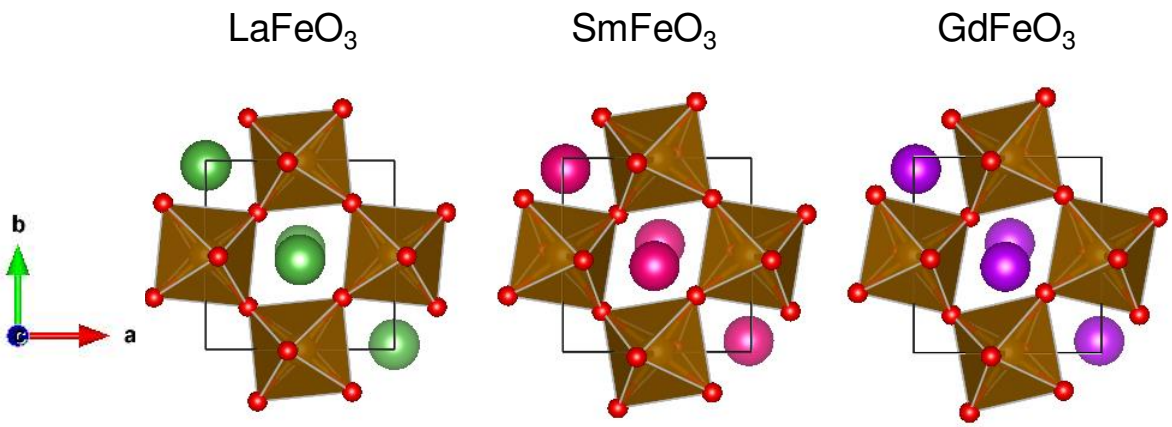

Figure 6. Polyhedral schematic of (La,Sm,Gd)FeO_3 orthorhombic perovskites along axis *c*, rendered in VESTA © [24]. Lattice parameters are shown in Table 1.

4.2 Raman Spectroscopy

Raman spectra for all $LnFeO_3$ perovskites present bands consistent with those expected from literature as shown in Table 2. They also show agreement with the detailed Raman scattering study by Weber and colleagues [19]. There are 24 Raman-active modes in the space group *Pbnm* for rare-earth orthoferrites, which can be described by the representation $\gamma_{Raman,Pbnm}$: $7A_g+5B_{1g}+7B_{2g}+5B_{3g}$ [18]. Peaks at Raman shifts greater than ca. 700 cm^{-1} are reportedly not due to active modes, but rather to other phenomena; those at 1150 – 1200 and 1300 cm^{-1} are attributable to second order excitations of active modes [17,43], one-phonon scattering or two-phonon scattering [36,44]. Peaks observed around 650 cm^{-1} are believed to be caused by impurity scattering [44,45] or second-order Raman scattering [46]. Concerning the second phase in $GdFeO_3$, the main Raman peaks for yttria-stabilised zirconia (YSZ) appear around 266 ($Zr\text{-}O_{II}$ bending) and 645 cm^{-1} ($Zr\text{-}O_{I}$ stretching) [47], both of which can also be attributed to $GdFeO_3$ itself. We observe a greater intensity of the 647 cm^{-1} Raman peak, which may be caused by the low level of YSZ contamination in this sample.

From the crystal structures of these perovskites, and the refined lattice parameters in Table 1, a change is observed in the angles of bonds through which the FeO_6 octahedra connect by corner-sharing oxygen atoms, indicating that their relative tilts vary. Vibrational modes $A_g(3)$ and $A_g(5)$ are associated with the [010] and [101] rotations respectively, i.e. in the direction of *c* and of *a* and *b*. Weber and colleagues, in 2016 [19], presented the Raman band positions for these vibrational modes, as illustrated in Table 4. Weber comment on the linear trends between the band positions of these vibration modes, and the angle octahedra rotational angle.

Table 4. Raman band positions for $A_g(3)$ and $A_g(5)$ from this work, and read from graphs presented by Weber et al. [19]

	This work (cm^{-1})		**Weber et al. (cm^{-1})** [19]	
	$A_g(3)$ [010]	**$A_g(5)$ [101]**	**$A_g(3)$ [010]**	**$A_g(5)$ [101]**
$LaFeO_3$	140 (5)	295 (5)	130 (10)	300 (10)
$NdFeO_3$	216 (5)	346 (5)	210 (10)	340 (10)
$SmFeO_3$	229 (5)	372 (5)	230 (10)	380 (10)
$EuFeO_3$	235 (5)	383 (5)	230 (10)	390 (10)
$GdFeO_3$	260 (5)	396 (5)	250 (10)	400 (10)

4.3 Mössbauer Spectroscopy and Debye Temperature Approximations

The temperature dependence of Centre Shift (CS) in Mössbauer spectra can be predicted by the Debye model for a given material, allowing variable temperature Mössbauer spectroscopy studies to approximate the Debye temperature [48], and by extension, the recoil-free fraction [49–51]. The recoil-free fraction, *f* factor, or Lamb-Mössbauer factor, is the temperature-dependent ratio of the recoilless γ absorption of a material, therefore the greater the *f* factor, the greater the Mössbauer spectral

area by comparison with a material with a smaller *f* factor. Ascertaining the recoil-free fraction of Fe within a particular phase enables quantification of its abundance in a mixed-phase material, which can be vital for studying materials that undergo phase changes, redox reactions or other forms of dynamic in-application, such as catalysis [49]. The Debye temperature of a material can also be used in further approximations of properties reliant on its thermal behaviour, such as specific heat capacity [52]. Debye temperatures for $LnFeO_3$ perovskites have been obtained previously through the temperature dependence of the Mössbauer Centre Shift [53] and through specific heat methods [54].

The Mössbauer spectra for all studied perovskites can be reliably fitted using a single sextet, indicating their magnetic nature as antiferromagnetic [21] with Centre Shift values consistent with octahedral Fe^{3+} [30,49]. The room temperature Centre Shifts for the $LnFeO_3$ series show little change as a function of the rare earth cation. A decrease in the magnitude of the internal magnetic field is observed, wherein B_{hf} is greatest for $LaFeO_3$ and decreases towards $GdFeO_3$, a trend shown to continue to $LuFeO_3$ by Eibschütz, Shtrikman and Treves [53]. which can be linked to the known decrease in Néel temperature of $LnFeO_3$ perovskites from La to Lu .From the refined structural data of the materials studied here, Fe-O bond lengths, and FeO_6 volumes, do not reflect the near-linear trend in B_{hf}, suggesting that these bond lengths are not a deciding factor in the magnitude of B_{hf}. The structural data of several $LnFeO_3$, from Pr to $LuFeO_3$ by Marezio, Remeika and Dernier in 1970 [34] show that through this series, the average distance between iron and rare earth atom decreases from Pr to Lu, as the Ln ionic radius decreases, and the difference in individual distances becomes greater. This could suggest that the proximity of Ln and Fe atoms, and the interactions between them, is influencing the magnitude of the hyperfine field of the iron. Links have also been made between the hyperfine field and the angles between magnetic domains [53].

Centre Shift and hyperfine magnetic field for all studied $LnFeO_3$ samples show non-linear increases with decreasing temperature. Increases in the hyperfine magnetic fields are due to the removal of thermal vibrations with reduced temperature, while the increases in the centre shift values can be explained using equations from the Debye model [53,55]. The stated centre shift values differ from the intrinsic isomer shift values as the centre shift is affected by temperature while isomer shift is an inherent parameter for a given material. The different values are brought about through the Second Order Doppler Shift (SODS) such that [48,56,57];

$$CS(\Theta_D, T) = IS + SODS(\Theta_D, T) \qquad \text{Equation (2)}$$

The Centre Shift (CS) is the experimentally observed outcome, while the Isomer Shift (IS) is temperature independent and a characteristic of the material, and the SODS is the temperature dependant term of this equation. The SODS can be related to the Debye temperature, and measured temperature by:

$$SODS = -\frac{3}{2}\frac{k\,\Theta_D}{Mc}\left[\frac{3}{8} + 3\left(\frac{T}{\Theta_D}\right)^4 \int_0^{\frac{\Theta_D}{T}} \frac{x^3 dx}{e^x - 1}\right] \qquad \text{Equation (3)}$$

where *k* is the Boltzmann constant; E_γ is the energy of the gamma ray (14.41 keV); *c* is the speed of light; θ_D is the Debye temperature; M is the mass of the iron, taken as 57 amu (multiplied by Avogadro's constant for conversion to mass). From this, the Debye temperature can be used to calculate the recoil-free fraction;

$$Lnf = -\frac{3E\gamma^2}{Mc^2 k\,\Theta_D}\left[\frac{1}{4} + \left(\frac{T}{\Theta_D}\right)^2 \int_0^{\frac{\Theta_D}{T}} \frac{x dx}{e^x - 1}\right] \qquad \text{Equation (4)}$$

In approximating the Debye temperature of a material, through the use of variable temperature Mössbauer spectroscopy, it is necessary to consider all temperature points simultaneously. A self-feeding program was constructed, in which a Debye temperature and an isomer shift would be simulated, resulting in theoretical SODS and Centre Shift. The objective of the program was to minimise the difference between the theoretical centre shift using simulated Debye temperatures and Isomer Shifts, for all measured temperatures simultaneously. The Debye temperature and Isomer Shift stipulated by the program, with the minimal difference between theoretical and experimental values, are those presented herein. This is the Debye temperature used in equation (4) to ascertain the recoil-free fraction of each material at a given temperature. Using these equations, by inputting a range of Debye temperatures, several trends were drawn to compare the values gathered in this study to theoretical values as illustrated in Figure 7. This process is not to fit the data presented against a theoretical line from Figure 7, and these lines are principally to guide the approximation procedure. Approximating the Debye temperature in this manner has been shown to reliably produce accurate values by Dubiel and colleagues previously [51,58], and here, summarised in

Table 5 are corroborating Debye temperatures from other research groups' data Mössbauer spectroscopy data using the present method. The material presented by Aldon was $LiFePO_4$, by Cieślak was σ-phase $Fe_{54}Cr_{46}$ and by Kim was $CoFe_2O_4$.

Table 5. Validation of Debye temperature and recoil-free fraction calculation method using third-party published data.

	θ_D (K) (This work)	θ_D Ref.	f_{293} (This work)
Aldon $LiFePO_4$ [50]	336 (10)	336	0.69 (2)
Cieślak $Fe_{54}Cr_{46}$ [58]	435 (10)	437 (7)	0.80 (2)
Kim $CoFe_2O_4$ Site A [59]	738 (10)	734 (5)	0.92 (2)

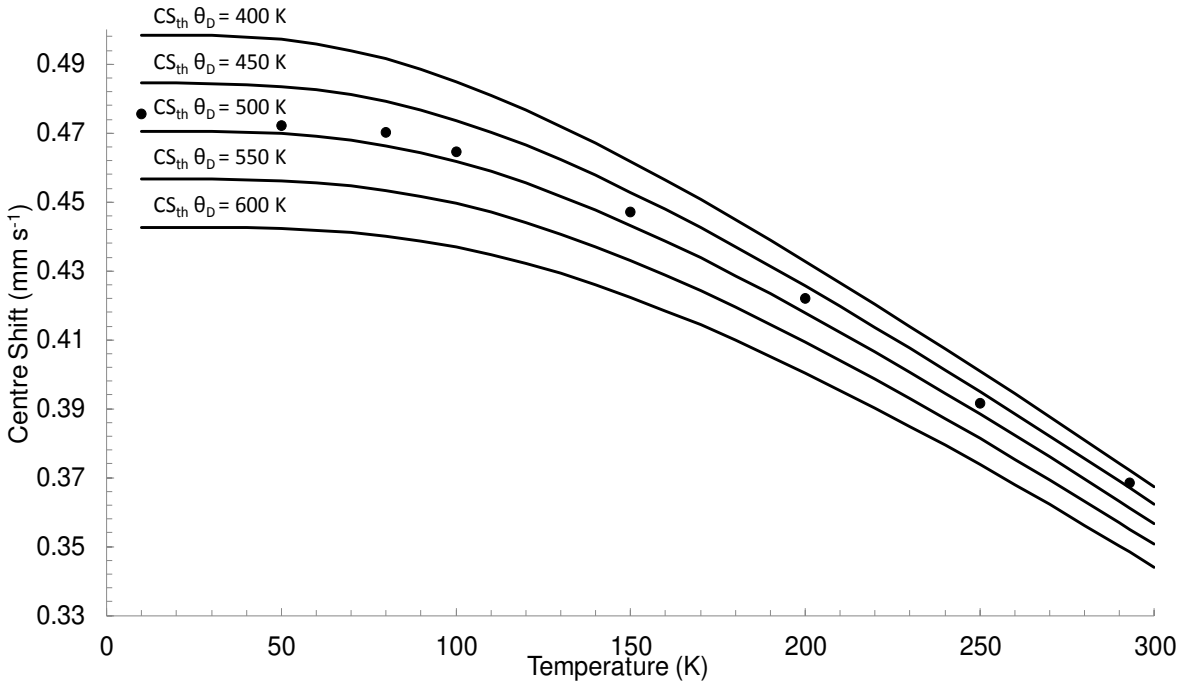

Figure 7. Theoretical trend lines of Centre Shifts for given θ_D (solid lines) and experimental data for $LaFeO_3$ (circles)with intrinsic Isomer Shift = 0.61 mm s^{-1}.

Table 6. Debye temperatures and recoil-free fractions for $LnFeO_3$ series with previously published data for comparison.

	θ_D / K (This work)	θ_D / K [53] (Eibshütz)	θ_D / K [54] (Parida)	θ_D / K [60] (Romero)	θ_D / K [61] (Morishita)	θ_D / K [62] (Yoon)
Method	Temp shift	Temp shift	Heat capacity	Elastic modulus	Heat capactiy	Temp shift
$LaFeO_3$	474 (20)	800 (50)	582	415	479	610
$NdFeO_3$	459 (20)	770 (50)	574			
$SmFeO_3$	457 (20)	730 (50)				
$EuFeO_3$	452 (20)	730 (50)		505		
$GdFeO_3$	473 (20)	770 (50)	555			

5. Discussion

The calculated Debye temperatures for the $LnFeO_3$ series are consistently ca. 300 K lower than those reported by Eibshütz [53], and are closer in value with values ascertained by other methods as shown in Table 6. When considering the differences observed between sources in Table 6, it is important to consider the methods by which the Debye temperatures were determined. It is known that the value of the Debye temperature depends on the method used to approximate it [58,63], and such comparisons of Debye temperatures are ideally made with values obtained using the same method and within the same temperature range. When using the data presented by Eibshütz [53] in the approximation program used in the present work, we obtain Debye temperatures considerably lower than the Debye temperatures reported by Eibshütz and closer to those obtained in this work, as shown in Table 7. Data for $EuFeO_3$ and $GdFeO_3$ were not used here as only two of Eibshütz's measured temperatures were within our measured range. The discrepancies in values that remain may be attributable to the improvements in spectroscopy equipment in the last 50 years that allow for more accurate measurements of the Centre Shift. It is certainly conceivable that the spectral noise of the data Eibshütz analysed and published, combined with their methodology of using a ruler to obtain Centre Shift values from spectra printed with chart recorder, could have introduced uncertainties into their data. Despite these differences, the overall trend in Debye temperatures from Ln = La to Gd, for our data, do follow the trend shown by Eibshütz wherein there is a reduction in Debye temperature from $LaFeO_3$ to $EuFeO_3$, and an increase for $GdFeO_3$.

Table 7. Debye temperature values obtained using the present method for $LnFeO_3$ materials using centre shift values from this work and from Eibshütz [53].

	θ_D K (This work)	θ_D K [53] (Eibshütz)
$LaFeO_3$	474 (10)	603 (10)
$NdFeO_3$	459 (10)	599 (10)
$SmFeO_3$	457 (10)	605 (10)

From these Debye temperatures, we find the recoil-free fractions for the $LnFeO_3$ perovskites from equation (4) as presented in Table 8. These values are not relative to α-Fe, as is often presented, and are the recoil-free fractions of these phases alone. The recoil-free fractions of these materials has been found to be greater than that of α-Fe previously, by comparing the spectral areas of suitable Mössbauer absorbers [64]. An *f*-factor that is greater than that of α-Fe implies that the iron nucleus is more strongly embedded, allowing for the recoilless absorption of γ-rays. It is suggested that the structure of these materials, wherein the iron is octahedrally co-ordinated in FeO_6 by ionic bonds, should be more thermally stable than α-Fe which is packed densely in planes bound by metallic bonds that allow for heat transfer more readily.

Table 8. Room temperature recoil-free fractions of $LnFeO_3$ series where Ln = La, Nd, Sm, Eu, Gd.

Orthoferrite	Room temperature recoil-free fraction ($f_{293\,K}$)
$LaFeO_3$	0.827 (20)
$NdFeO_3$	0.817 (20)
$SmFeO_3$	0.816 (20)
$EuFeO_3$	0.812 (20)
$GdFeO_3$	0.826 (20)

The simplest form of presenting the Debye temperature can be seen in equation (5) In this form we see both Planck'sand Boltzmann's constant, and only the variable Debye frequency, which is expressed in equation (6)

$$\theta_D = \frac{\mathrm{h}\nu_m}{k} \qquad \text{Equation (5) [55]}$$

$$\nu_m = \left(\frac{3N}{4\pi V}\right)^{1/3} \nu_S \qquad \text{Equation (6) [65]}$$

Through equations (5) and (6) it is shown that the Debye temperature of a crystal is related to the number density (N) of, and speed of sound (V) through, the crystal. The Debye frequency (v_m) is the characteristic frequency of a material, the maximum vibrational frequency, achieved due to a single normal vibration. The Debye temperature is the temperature of the crystals highest normal mode of vibration [55,65]. As the recoil-free fraction relies on the ability the nucleus to absorb and fluoresce γ-rays, we find that an increase in v_m, and therefore an increase in the Debye temperature, resulting in an increase in *f* is to be expected. An increase in Debye temperatures reflects an increase in the rigidity of the FeO_6 octahedra in the $LnFeO_3$. This can be taken from the relationship observed between FeO_6 octahedra volumes and Fe-O bond lengths, and Debye temperatures The approximated Debye temperatures in this work show an overall trend where θ_D decreases from $LaFeO_3$ to $EuFeO_3$, and $GdFeO_3$ sharply increases to a value near that of $LaFeO_3$, which agrees with the overall trend observed by Eibshütz and colleagues [53].

5. Conclusions

A series of $LnFeO_3$ perovskite oxides was synthesised through stoichiometric ball milling of oxide precursors, where Ln = La, Nd, Sm, Eu and Gd. ^{57}Fe Mössbauer spectroscopy measurements were taken at temperatures from 10 to 293 K. Debye temperatures and recoil-free fractions were calculated using equations relating the temperature dependence of the second ordering doppler shift and the centre shift of the Mössbauer spectra. The accuracy in temperature control and data processing allowed for the Debye temperatures calculated by this method to be consistent with heat capacity and relative Mössbauer spectral area methods, while allowing the observation of potential transitions that may occur over the temperature range. The

calculated Debye temperatures were complemented by translatable trends observed in Raman spectra, wherein greater intensities of Ln-O vibrations were presented by perovskites with lower Debye temperatures. This work provides suitable reference data on these rare earth orthoferrites which should prove useful in further studies investigating their structures, whether crystallographic or hyperfine, at ambient temperature or below, when studying their multitude of potential applications.

Acknowledgements

The authors wish to thank Dr Peter Ellis and Dr Kerry Simmance for their valuable input and useful discussions. The authors also thank the anonymous reviewers for their insightful observations and constructive suggestions.

1. Niu X, Li H, Liu G. Preparation, characterization and photocatalytic properties of $REFeO_3$ (RE=Sm, Eu, Gd). J Mol Catal A Chem. 2005;232:89–93.

2. Sora IN, Fontana F, Passalacqua R, Ampelli C, Perathoner S, Centi G, et al. Photoelectrochemical properties of doped lanthanum orthoferrites. Electrochim Acta [Internet]. 2013;109(3):710–5. Available from: http://dx.doi.org/10.1016/j.electacta.2013.07.132

3. Berry FJ, Ren X, Marco JF. Reduction properties of perovskite-related rare earth orthoferrites. Czechoslov J Phys. 2005;55(7):771–80.

4. Russo N, Mescia D, Fino D, Saracco G, Specchia V. N_2O Decomposition over Perovskite Catalysts. Ind Eng Chem Res [Internet]. 2007 Jun 1;46(12):4226–31. Available from: http://dx.doi.org/10.1021/ie0612008

5. Duprez D, Can F, Courtois X, Batiot-dupeyrat C, Laassiri S, Alamdari H. Perovskites as Substitutes of Noble Metals for Heterogeneous Catalysis : Dream or Reality Se b. Chem Rev. 2014;114:10292–368.

6. Arakawa T, Kurachi H, Shiokawa J. Physicochemical properties of rare earth perovskite oxides used as gas sensor material. J Mater Sci [Internet]. 1985 Apr;20(4):1207–10. Available from: https://doi.org/10.1007/BF01026315

7. Wang X, Qin H, Pei J, Chen Y, Li L, Xie J, et al. Sensing performances to low concentration acetone for palladium doped $LaFeO_3$ sensors. J Rare Earths [Internet]. 2016;34(7):704–10. Available from: http://dx.doi.org/10.1016/S1002-0721(16)60082-0

8. Minh NQ. Ceramic Fuel Cells. J Am Ceram Soc [Internet]. 1993;76(3):563–88. Available from: http://dx.doi.org/10.1111/j.1151-2916.1993.tb03645.x

9. Artyukhin S, Mostovoy M, Jensen NP, Le D, Prokes K, De Paula VG, et al. Solitonic lattice and Yukawa forces in the rare-earth orthoferrite $TbFeO_3$. Nat Mater. 2012;11(8):694–9.

10. Sławiński W, Przeniosło R, Sosnowska I, Suard E. Spin reorientation and structural changes in $NdFeO_3$. J Phys Condens Matter [Internet].

2005;17:4605–14. Available from: http://stacks.iop.org/0953-8984/17/i=29/a=002?key=crossref.79f51b441b87dfb04e266b28aa7992ff

11. Tyunina M, Yao L, Chvostova D, Dejneka A, Kocourek T, Jelinek M, et al. Concurrent bandgap narrowing and polarization enhancement in epitaxial ferroelectric nanofilms. Sci Technol Adv Mater. 2015;16(2).

12. Uchino K. Glory of piezoelectric perovskites. Sci Technol Adv Mater. 2015;16(4).

13. Labhasetwar N, Saravanan G, Kumar Megarajan S, Manwar N, Khobragade R, Doggali P, et al. Perovskite-type catalytic materials for environmental applications. Sci Technol Adv Mater. 2015;16(3).

14. Yang S, Fu W, Zhang Z, Chen H, Li C-Z. Recent advances in perovskite solar cells: efficiency, stability and lead-free perovskite. J Mater Chem A [Internet]. 2017;5(23):11462–82. Available from: http://xlink.rsc.org/?DOI=C7TA00366H

15. Kubicek M, Bork AH, Rupp JLM. Perovskite oxides – a review on a versatile material class for solar-to-fuel conversion processes. J Mater Chem A [Internet]. 2017;5(24):11983–2000. Available from: http://xlink.rsc.org/?DOI=C7TA00987A

16. Mitchell RH. Perovskites: Modern and Ancient [Internet]. Almaz Press; 2002. Available from: https://books.google.co.uk/books?id=8RF-QgAACAAJ

17. Romero M, Gómez RW, Marquina V, Pérez-mazariego JL, Escamilla R. Synthesis by molten salt method of the $AFeO_3$ system (A = La , Gd) and its structural , vibrational and internal hyper fi ne magnetic fi eld characterization. 2014;443(Figure 1):90–4.

18. Gupta HC, Kumar Singh M, Tiwari LM. Lattice dynamic investigation of Raman and infrared wavenumbers at the zone center of orthorhombic $RFeO_3$ (R = Tb, Dy, Ho, Er, Tm) perovskites. J Raman Spectrosc [Internet]. 2002;33(1):67–70. Available from: http://dx.doi.org/10.1002/jrs.805

19. Weber MC, Guennou M, Zhao HJ, Íñiguez J, Vilarinho R, Almeida A, et al. Raman spectroscopy of rare-earth orthoferrites $RFeO_3$ (R = La, Sm, Eu, Gd, Tb, Dy). Condens Matter Mater Sci [Internet]. 2016;3:1–9. Available from: http://arxiv.org/abs/1609.07987

20. Geller S, Wood E a. Crystallographic studies of perovskite-like compounds. I. Rare earth orthoferrites and $YFeO_3$, $YCrO_3$, $YAlO_3$. Acta Crystallogr [Internet]. 1956;9(1954):563–8. Available from: http://scripts.iucr.org/cgi-bin/paper?S0365110X56001571

21. Niwa E, Sato T, Watanabe Y, Toyota Y, Hatakeyama Y, Judai K, et al. Dependence of crystal symmetry , electrical conduction property and electronic structure of $LnFeO_3$ (Ln : La , Pr , Nd , Sm) on kinds of Ln^{3+}. J Ceram Soc Japan. 2015;3:501–6.

22. Huízar-Félix AM, Hernández T, de la Parra S, Ibarra J, Kharisov B. Sol-gel based Pechini method synthesis and characterization of $Sm_{1-x}Ca_xFeO_3$

perovskite 0.1≤x≤0.5. Powder Technol [Internet]. 2012;229:290–3. Available from: http://dx.doi.org/10.1016/j.powtec.2012.06.057

23. Grabowska E. Selected perovskite oxides: Characterization, preparation and photocatalytic properties-A review. Appl Catal B Environ [Internet]. 2016;186:97–126. Available from: http://dx.doi.org/10.1016/j.apcatb.2015.12.035

24. Momma K, Izumi F. VESTA: A three-dimensional visualization system for electronic and structural analysis. J Appl Crystallogr. 2008;41(3):653–8.

25. Coppens P, Eibschütz M. Determination of the crystal structure of yttrium orthoferrite and refinement of gadolinium orthoferrite. Acta Crystallogr [Internet]. 1965;19(4):524–31. Available from: http://scripts.iucr.org/cgi-bin/paper?S0365110X65003833

26. Tang P, Zhang J, Fu M, Cao F, Lv C. Characterization and Preparation Nanosized $CeFeO_3$ by a Microwave Process. Integr Ferroelectr [Internet]. 2013;146(July 2015):99–104. Available from: http://www.tandfonline.com/doi/abs/10.1080/10584587.2013.789756

27. Bedekar V, Jayakumar OD, Manjanna J, Tyagi a. K. Synthesis and magnetic studies of nano-crystalline $GdFeO_3$. Mater Lett. 2008;62:3793–5.

28. Rietveld HM. A profile refinement method for nuclear and magnetic structures. J Appl Crystallogr [Internet]. 1969;2(2):65–71. Available from: http://scripts.iucr.org/cgi-bin/paper?S0021889869006558

29. Rodriguez-carvajal J. Recent advances in magnetic structure determination by neutron powder diffraction. Phys B. 1993;192:55–69.

30. Kovats T a., Walker JC. Mössbauer absorption in Fe^{57} in metallic iron from the curie point to the - Transition. Phys Rev. 1969;181(1963):610–8.

31. Rancourt D. Recoil Mössbauer Spectral Analysis Software. 1998.

32. Tsybulya S V, Shmakov AN, Kryukova GN, Yakovleva IS, Isupova LA. High temperature studies of $La_{1-x}Sr_xFeO_{3-d}$ solid solutions using synchrotron radiation. J Struct Chem. 2007;48(6):1170–4.

33. Kuo CY, Drees Y, Fernández-Díaz MT, Zhao L, Vasylechko L, Sheptyakov D, et al. K=0 magnetic structure and absence of ferroelectricity in $SmFeO_3$. Phys Rev Lett. 2014;113(21):1–5.

34. Marezio M, Remeika JP, Dernier PD. The crystal chemistry of the rare earth orthoferrites. Acta Crystallogr Sect B Struct Crystallogr Cryst Chem [Internet]. 1970;26(12):2008–22. Available from: http://scripts.iucr.org/cgi-bin/paper?S0567740870005319

35. Nettleship I, Stevens R. Tetragonal zirconia polycrystal (TZP)-A review. Int J High Technol Ceram. 1987;3(1):1–32.

36. Lee WY, Yun HJ, Yoon JW. Characterization and magnetic properties of $LaFeO_3$ nanofibers synthesized by electrospinning. J Alloys Compd [Internet].

2014;583(3):320–4. Available from: http://dx.doi.org/10.1016/j.jallcom.2013.08.191

37. Chanda S, Saha S, Dutta A, Sinha TP. Raman spectroscopy and dielectric properties of nanoceramic $NdFeO_3$. Mater Res Bull [Internet]. 2013;48(4):1688–93. Available from: http://dx.doi.org/10.1016/j.materresbull.2012.12.075

38. Usman IB. Synthesis and characterization of Sm-based orthoferrite compounds, $SmFe_{1-x}Mn_xO_3$. 2010.

39. Ju L, Chen Z, Fang L, Dong W, Zheng F, Shen M. Sol-gel synthesis and photo-fenton-like catalytic activity of $EuFeO_3$ nanoparticles. J Am Ceram Soc. 2011;94(10):3418–24.

40. Shannon RD. Revised effective ionic radii and systematic studies of interatomic distances in halides and chalcogenides. Acta Crystallogr Sect A. 1976;32(5):751–67.

41. Martin U, Boysen H, Frey F. Neutron powder investigation of tetragonal and cubic stabilized zirconia, TZP and CSZ, at temperatures up to 1400 K. Acta Crystallogr Sect B. 1993;49(3):403–13.

42. Sato T, Takagi S, Deledda S, Hauback BC, Orimo SI. Extending the applicability of the Goldschmidt tolerance factor to arbitrary ionic compounds. Sci Rep [Internet]. 2016;6(April):1–10. Available from: http://dx.doi.org/10.1038/srep23592

43. Shim S-H, Duffy TS. Raman spectroscopy of Fe_2O_3 to 62 GPa. Am Mineral. 2001;87:318–26.

44. Popa M, Frantti J, Kakihana M. Lanthanum ferrite $LaFeO_{3+d}$ nanopowders obtained by the polymerizable complex method. Solid State Ionics. 2002;154–155:437–45.

45. Koshizuka N, Ushioda S. Inelastic-light-scattering study of magnon softening in $ErFeO_3$. Phys Rev B [Internet]. 1980 Dec;22(11):5394–9. Available from: https://link.aps.org/doi/10.1103/PhysRevB.22.5394

46. Podobedov VB, Weber A, Romero DB, Rice JP, Drew HD. Effect of structural and magnetic transitions in $La_{1-x}M_xMnO_3$ single crystals in Raman scattering. Phys Rev B [Internet]. 1998 Jul;58(1):43–6. Available from: https://link.aps.org/doi/10.1103/PhysRevB.58.43

47. Hemberger Y, Wichtner N, Berthold C, Nickel KG. Quantification of yttria in stabilized zirconia by Raman spectroscopy. Int J Appl Ceram Technol. 2016;13(1):116–24.

48. Herber RH. Structure, Bonding, and the Mossbauer Lattice Temperature. In: Herber RH, editor. Chemical Mössbauer Spectroscopy [Internet]. Boston, MA: Springer US; 1984. p. 199–216. Available from: https://doi.org/10.1007/978-1-4613-2431-7_8

49. Dyar MD, Agresti DG, Schaefer MW, Grant CA, Sklute EC. Mössbauer

Spectroscopy of Earth and Planetary Materials. Annu Rev Earth Planet Sci [Internet]. 2006;34(1):83–125. Available from: http://www.annualreviews.org/doi/10.1146/annurev.earth.34.031405.125049

50. Aldon L, Perea A, Womes M, Ionica-Bousquet CM, Jumas JC. Determination of the Lamb-Mössbauer factors of $LiFePO_4$ and $FePO_4$ for electrochemical in situ and operando measurements in Li-ion batteries. J Solid State Chem. 2010;183(1):218–22.

51. Dubiel SM, Cieślak J, Alenkina I V., Oshtrakh MI, Semionkin VA. Evaluation of the Debye temperature for iron cores in human liver ferritin and its pharmaceutical analogue, Ferrum Lek, using Mössbauer spectroscopy. J Inorg Biochem. 2014;140:89–93.

52. Kittel C. Phonons II. Thermal Properties. In: Introduction to Solid State Physics [Internet]. Wiley India Pvt. Limited; 2007. Available from: https://books.google.co.uk/books?id=F9Qu5c_hUaUC

53. Eibschütz M, Shtrikman S, Treves D. Mössbauer Studies of Fe^{57} in Orthoferrites. Phys Rev [Internet]. 1967;156(2):562–77. Available from: http://link.aps.org/doi/10.1103/PhysRev.156.562

54. Parida SC, Rakshit SK, Singh Z. Heat capacities, order-disorder transitions, and thermodynamic properties of rare-earth orthoferrites and rare-earth iron garnets. J Solid State Chem. 2008;181(1):101–21.

55. Hill TL. The Debye Approximation. In: An Introduction to Statistical Thermodynamics [Internet]. Dover Publications; 2012. (Dover Books on Physics). Available from: https://books.google.co.uk/books?id=gkldAwAAQBAJ

56. Herber RH, Smelkinson AE, Sienko MJ, Schneemeyer LF. Lattice dynamics in covalent solids: Sn in $SnS_{2-x}Se_x$($0 \leq x \leq 2$). J Chem Phys. 1978;68(8):3705–12.

57. Quinn JJ, Yi KS. Lattice Vibrations. In: Solid State Physics: Principles and Modern Applications [Internet]. Springer Berlin Heidelberg; 2009. Available from: https://books.google.co.uk/books?id=pf5DAAAAQBAJ

58. Cieślak J, Dubiel S, Żukrowski J, Reissner M, Steiner W. Determination of the Debye temperature of the σ-phase Fe-Cr alloys. Phys Rev B. 2002;65(21):1–3.

59. Kim SJ, Lee SW, Kim CS. Mössbauer Studies on Exchange Interactions in $CoFe_2O_4$. Jpn J Appl Phys [Internet]. 2001;40(Part 1, No. 8):4897–902. Available from: http://stacks.iop.org/1347-4065/40/4897

60. Romero M, Escamilla R, Marquina V, Gómez R. Structural and mechanic properties of $RFeO_3$ with R = Y, Eu and La perovskites: a first-principles calculation. Eur Phys J D. 2015;69(7).

61. Morishita M, Yamamoto H. Heat capacity of $La_{1-x}Sr_xFeO_{3-delta}$ from 2 K to 1340 K. Mater Trans [Internet]. 2007;48(12):3109–17. Available from: http://www.jstage.jst.go.jp/article/matertrans/48/12/48_3109/_article

62. Yoon SH, Choi SJ, Cha DJ, Min BK, Kim CS. Effects of Ga substitution in $LaFe_{1-x}Ga_xO_3$ (x = 0, 0.1, 0.3, 0.5 and 0.7). J Magn. 2002;7(2):40–4.

63. Wilson RH, Skelton EF, Katz JL. Measurement of the thermal variation of the X-ray Debye temperature of pure nickel and chromium. Acta Crystallogr [Internet]. 1966 Nov;21(5):635–8. Available from: https://doi.org/10.1107/S0365110X6600361X

64. Morales LA, Sierra-Gallego G, Barrero CA, Arnache O. Relative recoilless F-factors in $REFeO_3$ (RE = rare-earth La, Pr, Nd and Sm) orthoferrites synthesized by self-combustion method. Mater Sci Eng B Solid-State Mater Adv Technol [Internet]. 2016;211:94–100. Available from: http://dx.doi.org/10.1016/j.mseb.2016.06.005

65. Kestin J, Dorfman JR. A Course in Statistical Thermodynamics. New York: Academic Press; 1971. 577 p.

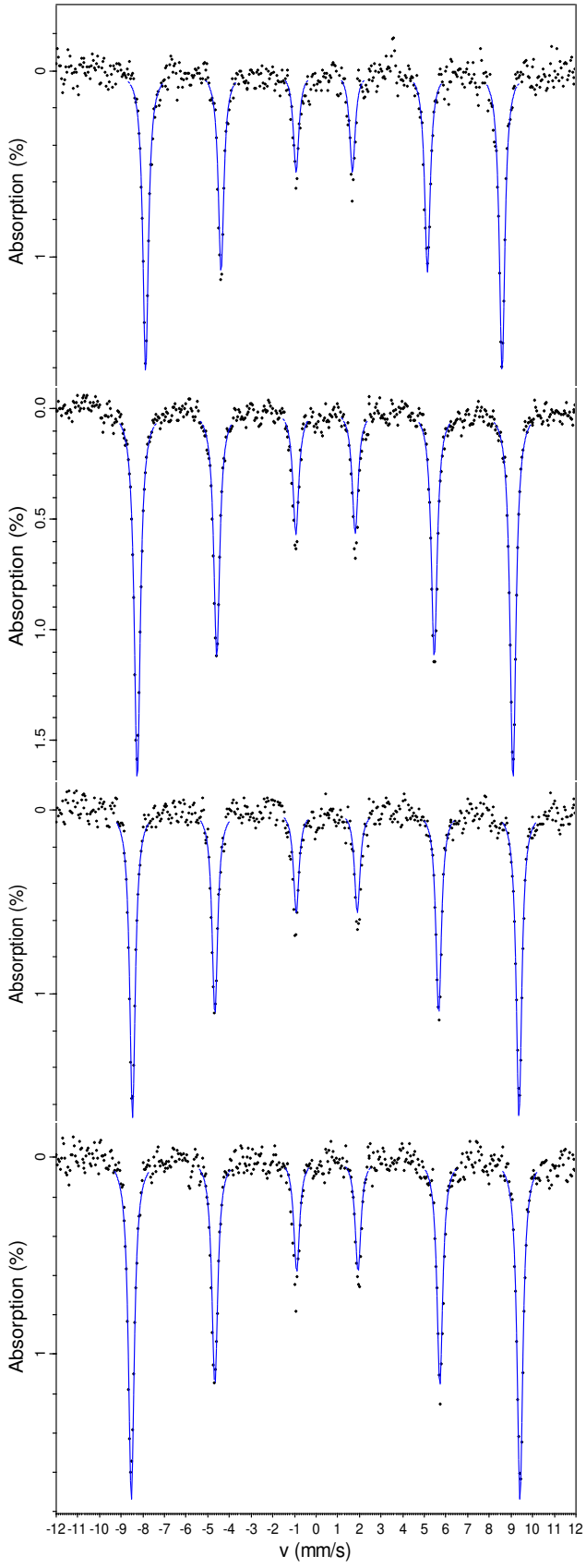

Figure 8. Fitted Mössbauer spectra of $NdFeO_3$ perovskite measured at 293, 200, 100 and 10 K (top to bottom).

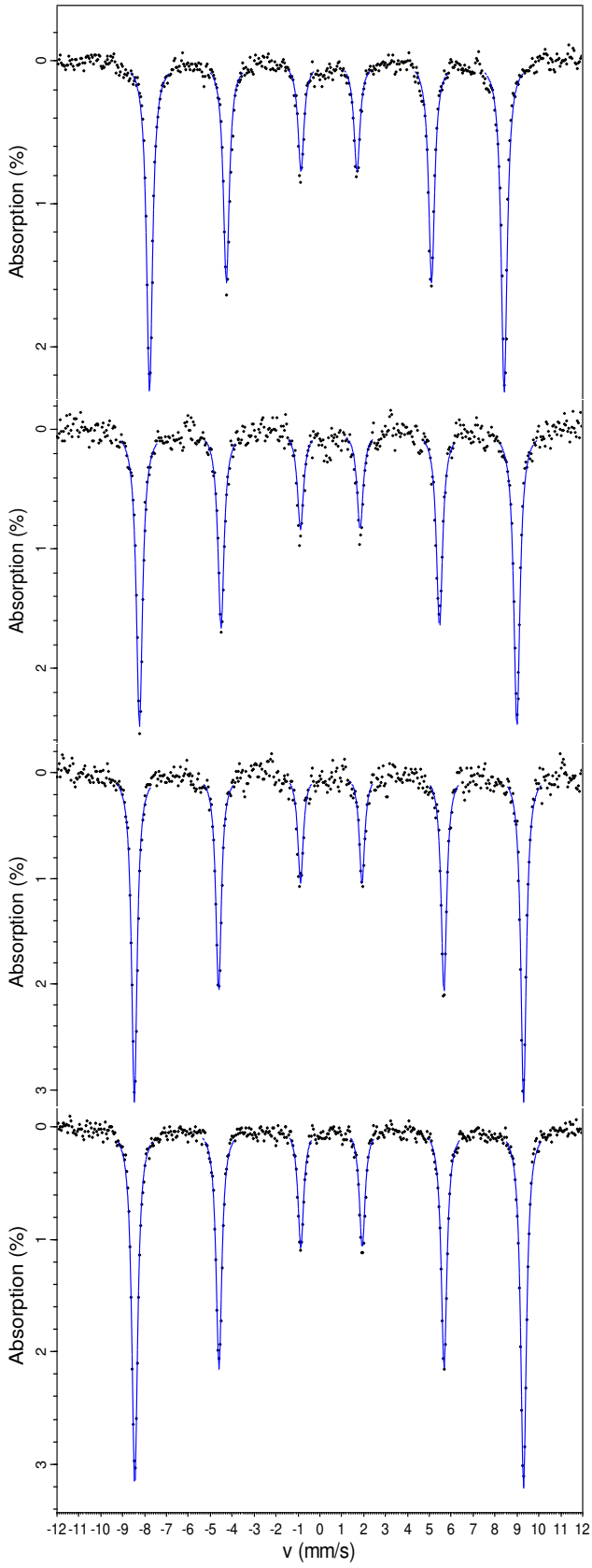

Figure 9. Fitted Mössbauer spectra of $SmFeO_3$ perovskite measured at 293, 200, 100 and 10 K (top to bottom).

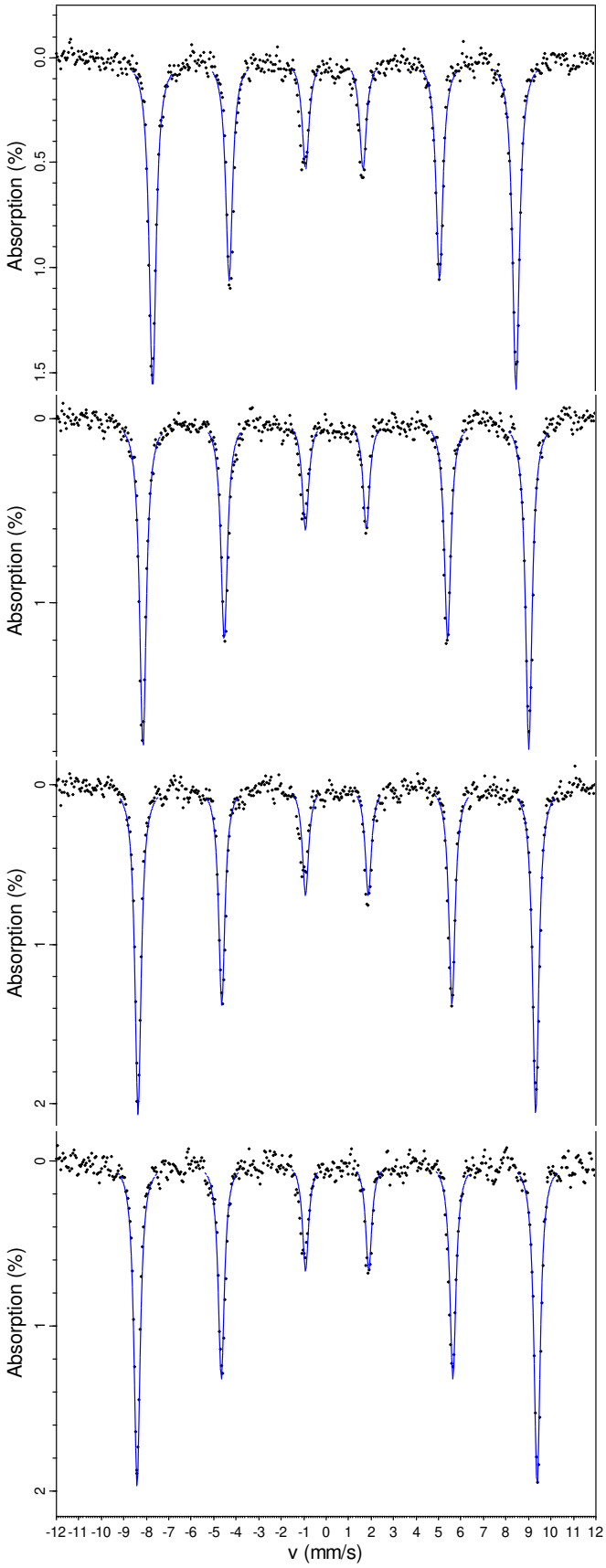

Figure 10. Fitted Mössbauer spectra of $EuFeO_3$ perovskite measured at 293, 200, 100 and 10 K (top to bottom).

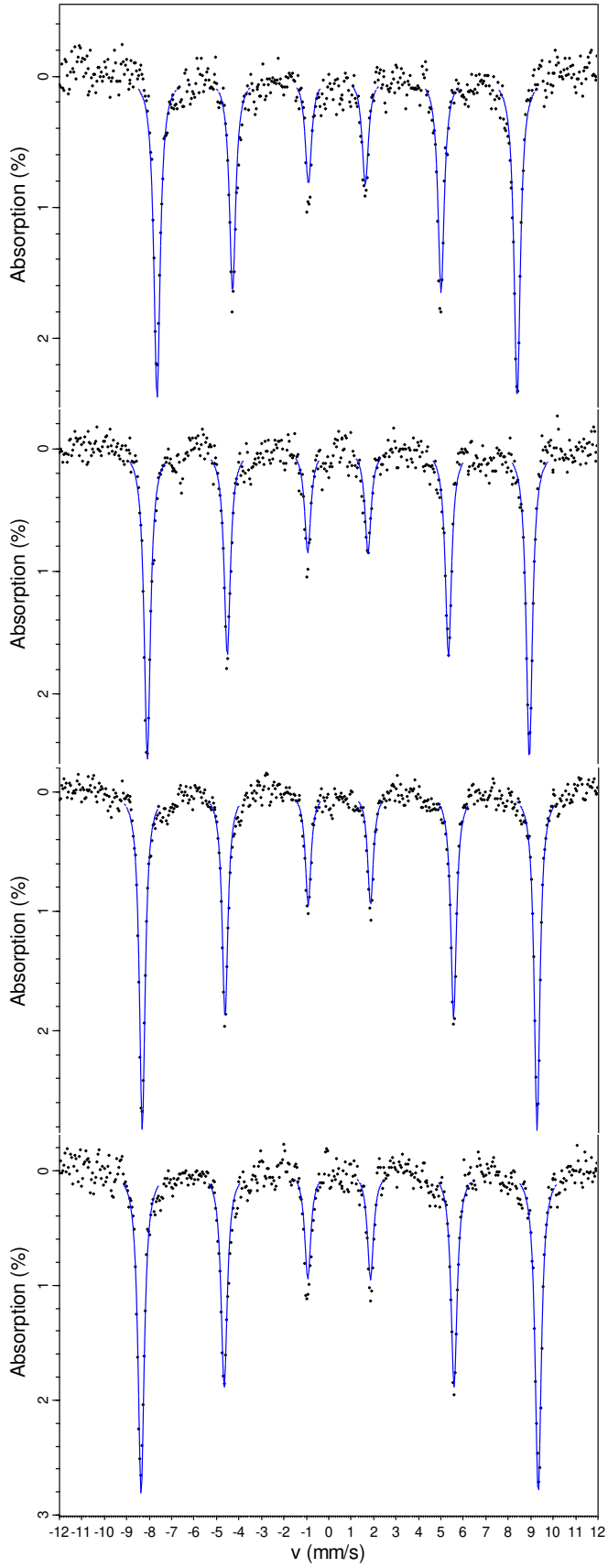

Figure 11. Fitted Mössbauer spectra of $GdFeO_3$ perovskite measured at 293, 200, 100 and 10 K (top to bottom).